EE

EUROPEAN ORGANIZATION FOR NUCLEAR RESEARCH

CERN - PS DIVISION

CERN/PS 94-02 (AR)

CONSOLIDATION OF THE 400 KA MAGNETIC HORN FOR AAC ANTIPROTON PRODUCTION

D. Boimond, M. Frauchiger, T. Kurtyka, M. Lubrano di Scampamorte
R. Maccaferri, S. Maury, L. Nikitina*, J.-C. Schnuriger

Abstract

A magnetic horn of biconical shape has been built as a back-up to the Lithium lens for the collection of antiprotons in the AAC to ensure the antiproton physics in the future.

This paper describes the design parameters, the shape and the wall thickness variations. It gives details of the mechanical stress analysis made using both analytical methods and finite element computation to optimize the thickness. Improvements to the pulsed power supply are also discussed as well as results obtained in laboratory and in operational conditions.

*Visiting Fellow - on leave of absence from IHEP, Protvino, Moscow.

Geneva, Switzerland
6/5/94

CONTENTS

INTRODUCTION

Antiprotons are produced in the target area, transferred through the Antiproton Collector (AC) to the Antiproton Accumulator (AA) for cooling and accumulation into a stack, from which bunches are extracted and transferred to the different users.

During Sp$\bar{p}$S physics runs, the performance of the AAC was of great importance for the collider luminosity. The design goal was to increase the accumulation rate by a factor of 10, with dense stacks of up to 10^{12} $\bar{p}$. Many improvements have been made in a large number of areas [1], in particular in the collection of antiprotons, where different collectors have been successfully used:

- A 20 mm diameter lithium lens, pulsed at 480 kA, was the main collector lens used operationally.
- Originally designed for 800 kA, a 36 mm diameter lithium lens pulsed at 1.2 MA was developed in collaboration with INP (Novosibirsk) and tested in the machine [2], but during a subsequent lifetime test in laboratory, the stainless steel container failed. A new 34 mm diameter lens with a stronger container has been made and operated at 1.0 MA.
- A 60 mm diameter magnetic horn [3] pulsed at 400 kA has been used during several operational periods.

The first magnetic horn [4] was designed to be pulsed at 160 kA in the old AA. The AC machine acceptance being higher, a stronger horn with a larger diameter was developed. This horn, of a biconical shape, was designed, built and tested directly in the machine in 1988. Its yield was ~15% lower than the 20 mm Li lens and it has pulsed several millions of shots.

The Sp$\bar{p}$S run collider physics was completed in 1991. Since 1991, the AAC has been running only for LEAR physics, which can be satisfied with a lower antiproton production. Magnetic horns are more advantageous than other collectors tbecause:

- they are simple (no chemically dangerous materials),
- they are efficient (used at the top current),
- they are light,
- the removable part (horn, strip line) is very cheap,
- their induced radioactivity is low (aluminium).

These advantages largely overhide the slightly smaller yield which is sufficient for the low energy antiproton physics.

All the difficulties and the efforts made to obtain spare magnetic horns with a sufficient reliability to be used in the future AAC runs where a relatively low-production yield is acceptable, are summarised in this paper.

The first chapter relates the horn design considerations with respect to the focusing, shape, magnetic field calculations and the general approach to mechanical stress calculations. The second chapter describes the mechanical studies realised on a computational model and on the final design of a horn 0.4 mm thicker than the original one. The third chapter describes the analysis done on the existing electrical pulser [9, 10] to study its improvement in order to reduce the stresses on the horn. Finally, the last chapter gives an overview of the experimental results obtained in the laboratory and in the real antiproton production conditions in the target area.

1. DESIGN OF THE 400 kA MAGNETIC HORN

1.1 Focusing

The shape of the magnetic horn used in the AA was designed to focus the highly diverging $\bar{p}$ beam from the production target into a beam of parallel trajectories (Fig. 1). The maximum angle to be collected by a magnetic horn varies by the square root of the current intensity, then the larger acceptance provided by the AC ring has required an increase of the horn current from 160 kA to 400 kA at least. Due to the larger electromagnetic forces and the resulting larger mechanical stresses, it has been necessary to change the AA horn design. A biconical shape having been proposed for intensity up to 250 kA [5], and having shown a very good reliability in laboratory tests, it was proposed to build a similar 400 kA horn, basically made of two cones connected by a short cylindrical tube [3]. The chosen shape allows easy access from the two sides for the machining and provides a focal length which does not vary with the trajectory angle.

A Mathcad^R program* [6] was used to determine the shape of the outer side of a biconical magnetic horn. For that purpose, the initial conditions needed were: current, magnetic rigidity, and values of the large and small radius.

$$I = 400 \text{ kA}; \quad B\rho = 11.9256 \text{ Tm}; \quad R_{max} = 30 \text{ mm}; \quad R_{min} = 6 \text{ mm}.$$

with a permeability of free space of $\mu_0 = 4\pi \times 10^{-7}$

The resulting characteristic angle is then given by:

$$\theta = \sqrt{\frac{\mu_0 I}{2\pi B\rho}} \quad \text{which gives } \theta = 81.9 \text{ mrad}$$

The focal length is therefore:

$$f = \frac{R_{max}}{\theta}, \quad f = 0.366 \text{ m}$$

---

* MATHEMATICA is a registred trademark, MATHCAD 4.0 is a trademark of Mathsoft Inc. Copyrights 1993-1996.

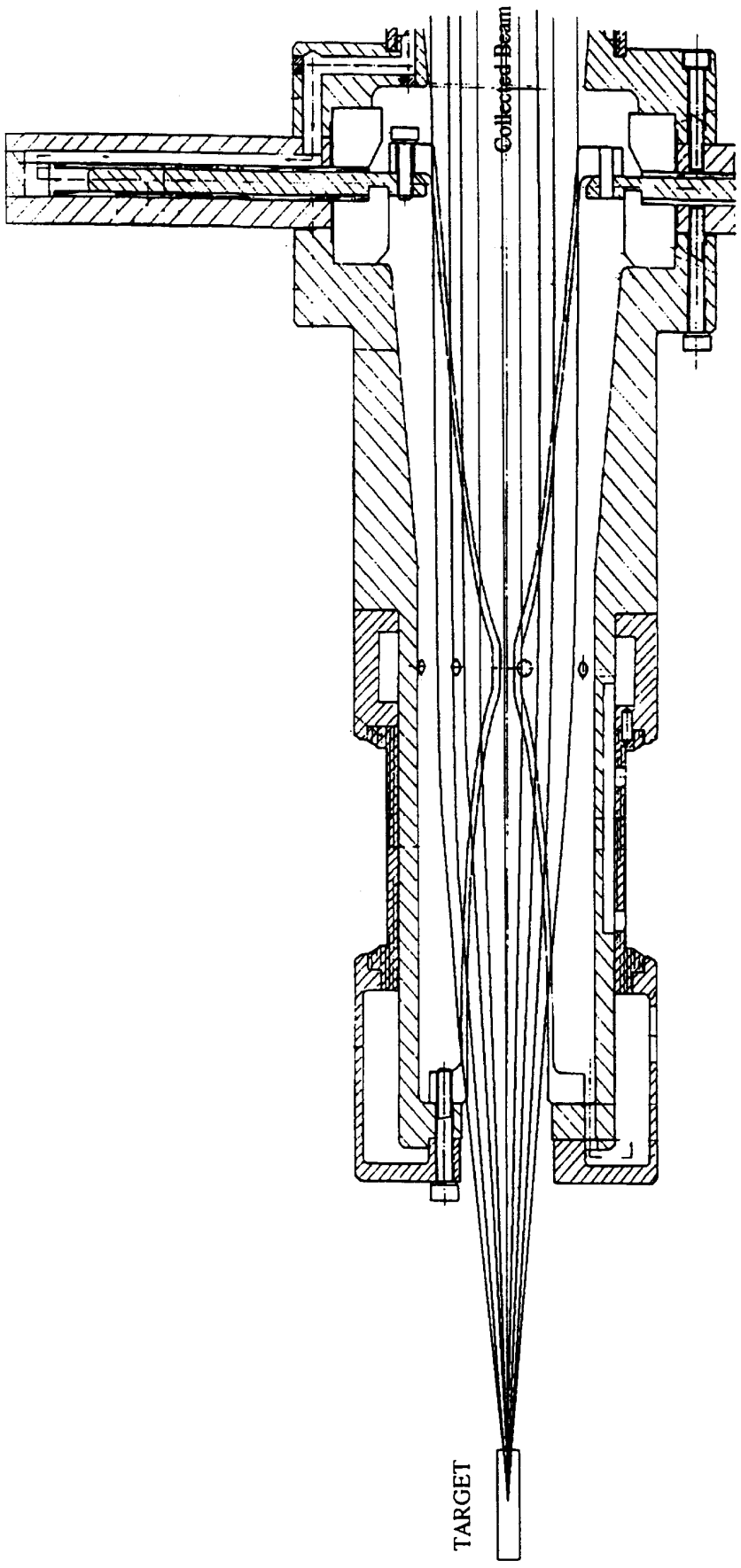

Figure 1 - Mechanical Horn assembly and schematic of beam focusing

The shape of the upstream cone is then given by the following three parametric equations [5]:

$$RRH(\alpha) = f \cdot \alpha \cdot \exp\left(-\frac{\alpha^2}{2\theta^2}\right)$$

$$RH(\alpha) = if\left(RRH(\alpha) > R_{min}, RRH(\alpha), R_{min}\right)$$

$$ZS(\alpha) = f \cdot \exp\left(-\frac{\alpha^2}{2\theta^2}\right)$$

where *RRH* holds for the theoretical shape, *RH* for the shape down to the minimum radius of the neck between the two cones, *ZH*, *ZS* are the distances from the focus and α the parametric angle (Fig. 2).

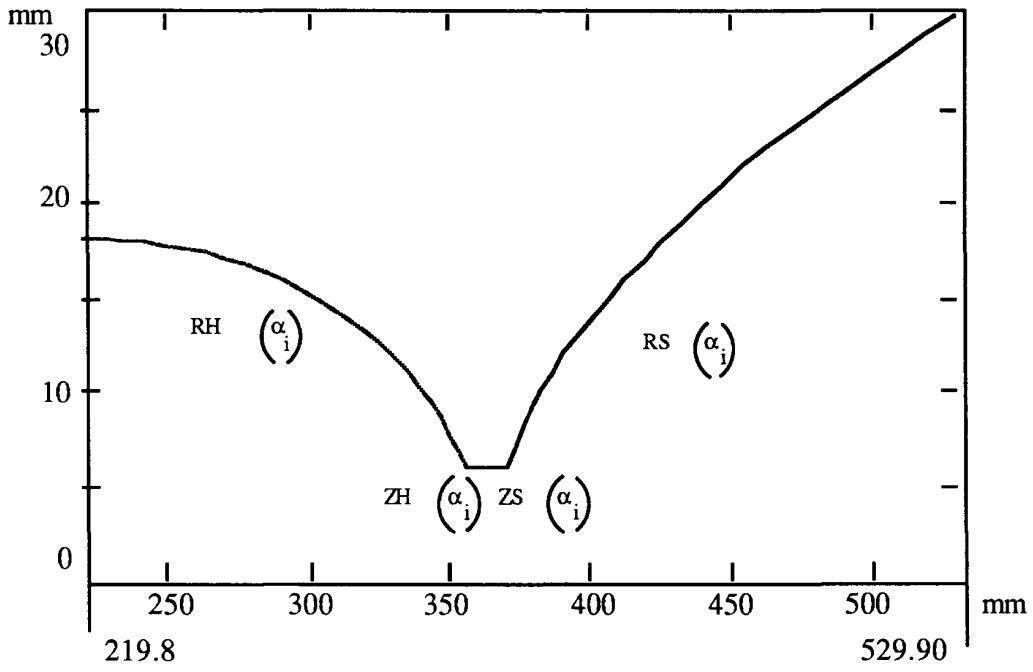

Fig. 2 - Theoretical shape of a biconical magnetic horn

Similarly, the dowstream cone is given by:

$$RRS(\alpha) = f \cdot \alpha$$

$$RS(\alpha) = if\left(RRS(\alpha) > R_{min}, RRS(\alpha), R_{min}\right)$$

$$ZS(\alpha) = f \cdot \exp\left(-\frac{\alpha^2}{2\theta^2}\right) + f \cdot \left(\frac{\alpha}{\theta}\right)\sqrt{\frac{\pi}{2}}\, erf\left(\frac{\alpha}{\sqrt{2}\,\theta}\right)$$

1.2 Electromagnetic Pressure

A magnetic horn is essentially a cylindrical metal tube loaded by a short electromagnetic force. It is useful to calculate first the order of magnitude of the stress by considering a hollow tube submitted to a varying external pressure. One considers first a cylindrical hollow conductor fed by a dc current of intensity I, the current density j being constant between the inner and outer radii R_0 and R_1.

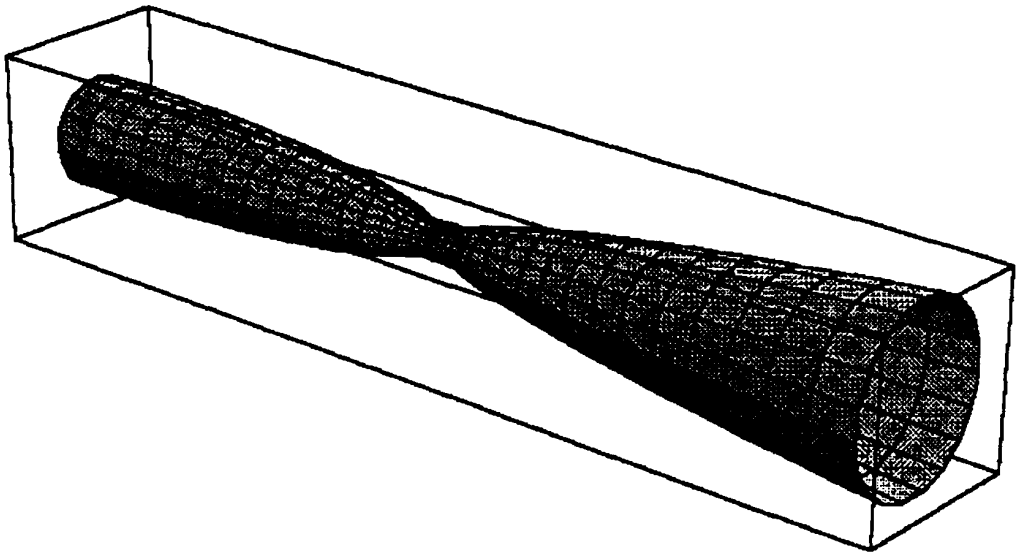

Fig. 3 - Perspective view of a biconical magnetic horn

The current passing through a cylinder of radius R between R_0 and R_1 is:

$$I(R) = j\pi\left(R^2 - R_0^2\right)$$

Applying the Ampere theorem:

$$B(R) = \frac{\mu_0 I(R)}{2\pi R}$$

On the external surface of the conductor:

$$I(R_1) = j\pi\left(R_1^2 - R_0^2\right)$$

which yields:

$$j = \frac{I(R_1)}{\pi\left(R_1^2 - R_0^2\right)}$$

The magnetic field inside the conductor is then:

$$B(R) = \frac{\mu_0 I(R_1)\left(R^2 - R_0^2\right)}{2\pi R\left(R_1^2 - R_0^2\right)}$$

Outside the conductor and inside another coaxial return conductor the field is:

$$B_{ext} = \mu_0 \frac{I(R_1)}{2\pi R_1}$$

One has also:

$$I = I(R_1)$$

The electromagnetic force F is a volume force given by the cross product $j*B$ for an elementary volume between two meridian planes, by summing up between R_0 and R_1 for one meter length.

$$F = \frac{\mu_0 I^2}{\left[2\pi^2\left(R_1^2 - R_0^2\right)^2\right]}\left[\left(\frac{R_1^3 - R_0^3}{3}\right) - R_0^2(R_1 - R_0)\right]$$

$$F = \frac{(R_1 + 2R_0)\mu_0 I^2}{6(R_1 + R_0)^2 \pi^2}$$

Assuming the material of the conductor is incompressible, the equivalent pressure on the external surface is then:

$$p = \frac{(R_1 + 2R_0)\mu_0 I^2}{6R_1(R_1 + R_0)^2 \pi^2}$$

By introducing the magnetic field on the outer suface:

$$p = \frac{2(R_1 + 2R_0)R_1}{3(R_1 + R_0)^2}\frac{B(R_1)^2}{\mu_0}$$

which yields for a thin tube ($R_0 \sim R_1$):

$$p = \frac{B(R_1)^2}{2\mu_0}$$

For a thick tube ($R_0 = 0$) the pressure becomes:

$$p = \frac{4}{3}\frac{B(R_1)^2}{2\pi_0}$$

It is clearly seen that replacing the electromagnetic force by an external pressure can lead to an underestimate of the effect of this force (this is equivalent to considering only one term in the Maxwell tensor).

A rigorous analysis of the mechanical stress differential equation would need to express the elementary volume force, and to solve the resultant differential equation. One considers here only the simple solutions as given in textbooks about elasticity and resistance of materials for the model of a thick cylinder, under an external pressure, and keeping a constant length.

Let us define

$$\Lambda = \frac{R_1^2}{R_0^2} - 1$$

Then, applying Timoshenko formulae

$$\sigma_t(R) = -\frac{p\left[\left(R_1^2/R_0^2\right)+\left(R_1^2/R^2\right)\right]}{\Lambda};\ \sigma_r(R) = -\frac{p\left[\left(R_1^2/R_0^2\right)-\left(R_1^2/R^2\right)\right]}{\Lambda};\ \sigma_z(R) = -\frac{p\left[\left(R_1^2/R_0^2\right)\right]}{\Lambda}$$

which are circumferential, radial and longitudinal terms.

These are compression stresses, the circumferential stress being always higher than the others and reaching a maximum value on the inner surface of the tube:

$$\sigma_{max} = p\frac{2R_0^2}{R_1^2 - R_0^2}$$

For a tube without a hole the maximum stress rises up to:

$$\sigma_{max} = 2p$$

For a thin tube (of thickness e):

$$\sigma_{max} = p\frac{R_1}{e}$$

The different following cases can be considered:

1) Conductor without a hole, dc current

$$\sigma_{max} = \frac{8}{3}\frac{B(R_1)^2}{2\mu_0}$$

2) Conductor without a hole, short pulse current:

$$\sigma_{max} = 2\frac{B(R_1)^2}{2\mu_0}$$

3) Hollow conductor:

$$\sigma_{max} = \frac{R_1}{e}\frac{B(R_1)^2}{2\mu_0}$$

but there may be buckling.

The preceding formulae give the order of magnitude of the maximum stress in a magnetic horn which can be compared with the maximum allowed stress in case of fatigue. In the case of vibrations or pulse loading, and for aluminium alloys these values are very inaccurate, hence long and careful tests are necessary. It is nevertheless interesting to consider the case of a holow conductor, and by introducing the field, this yields:

$$\sigma_{max} = \frac{\mu_0 I^2}{8\pi^2 e R_1}$$

In order to have a constant stress along the axis for a varying tube radius, the product eR_1 must be constant. This rule has been chosen in the case of the biconical magnetic horn, but this is no longer valid in the case of buckling for which the critical pressure is for a hollow and thin tube:

$$p_k = \frac{1}{4}\left[\frac{E}{1-\nu^2}\left(\frac{e}{R_1}\right)^3\right]$$

(E is the elasticity modulus, ν is the Poisson modulus)

from which, by introducing the current, the product e^3/R_1 must be constant.

In any case, this is approximate, because, in the case of the magnetic horn, the magnetic pressure is not uniform and the buckling mode is not known. The curvature of the surface along the axis and the proximity of the flanges improve the resistance to buckling.

1.3 Pulse Loading

The following remarks about pulse loading are relevant for a half-sine pulse and for the axisymmetric mode:

$$\sigma_{max}(\tau) = \frac{10^{-7} \times I^2}{2\pi R_1 e} \frac{\sin(\pi\tau)}{1-\tau^2}$$

where τ is the ratio of the pulse duration and the mechanical period (supposed to be <1). The variation of the pulse stress is given in Fig. 4.

This factor is proportional to τ for the small values of τ, from which one gets:

$$\sigma_{max}(\tau) = \frac{10^{-7} \times I^2}{2R_1 e}\tau$$

It is then better to minimize the pulse duration (this holds also to reduce the Joule heating). For the lower mechanical axisymmetric mode, the period is proportional to the radius, and therefore to the product eR_1^2, which should be kept constant. All these remarks apply to the case of the horn within the limits of the assumptions made and explain why the pulser has been improved.

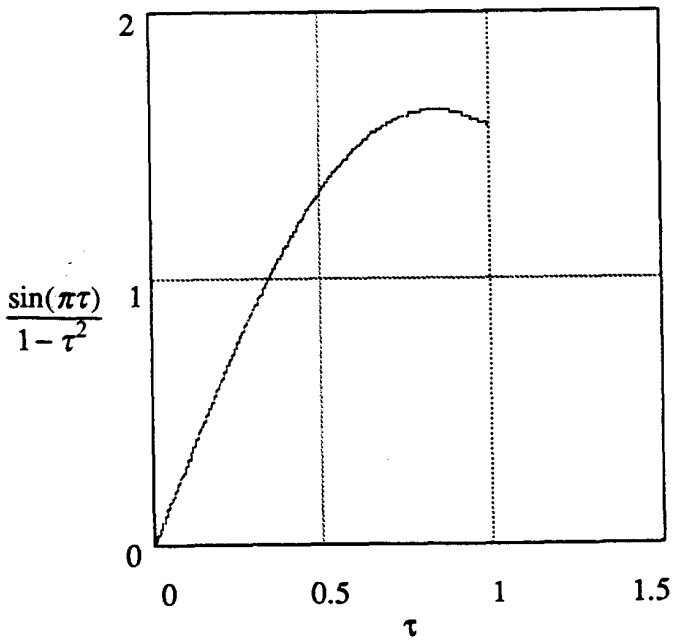

Fig 4 - Variation of the pulse stress versus T_P/T_M

Finally the longitudinal force applied on the radial connections between the inner conductor (radius R_1) and the external coaxial conductor (radius R_2) has to be considered. The current density in one of these connections is:

$$J_r(R) = \frac{I}{2\pi Rs}$$

where s is the current depth (along the axis).

The magnetic field is $B_{ext}(R)$ on the surface, as given previously; its mean value in s is half of that amount, from which the force density is:

$$\frac{\mu_0 I^2}{8\pi^2 R^2 s}$$

and the force between R and $R+dR$ is:

$$\frac{\mu_0 I^2}{8\pi^2 R^2 s} 2\pi R dR s$$

or

$$\frac{1}{4}\mu_0 \frac{I^2}{\pi R} dR$$

whose integral is

$$\frac{1}{4}\mu_0 \frac{I^2}{\pi} \ln(R)$$

and the total longitudinal force is then:

$$F_{long} = \frac{1}{4\pi}\mu_0 I^2 \ln\left(\frac{R_2}{R_1}\right)$$

The same force, but reversed, applies to the other connection of the central conductor. These forces are supported by the external conductor (whose thickness may be as large as needed) and by the central conductor which is therefore subject to axial stresses which add to the previously given axial stress. The stress due to the assembly tolerances and the thermal stresses due to Joule heating and the residual proton beam coming from the production target have to be added to these electromagnetic forces. A complete and careful analysis of all these effects needs finite element computation, but only long and methodical tests on prototypes can give reliable results and these are necessary anyway.

2. MECHANICAL ANALYSIS OF THE 400 kA MAGNETIC HORN

2.1 General Remarks

The main aim of the mechanical calculations was to check the dimensions of the magnetic horn, adapted for higher loading, with respect to instantaneous and fatigue strength. Following earlier practice [7] the present computations have been made using a simplified finite element model of the horn. The strength estimation is therefore merely comparative, based on previous calculations, on service records of old horns and on test results of the new horn variants. Two such variants have been tested and are included in the calculations:

1) Horn - Version A (thickness of thinnest parts equal to 1 mm, with the central part being 3 mm thick and 12 mm in diameter) - this was a preliminary design proposal, made with the aim to maximize the number of focused antiprotons, and therefore with the wall thickness being at the limit of mechanical strength. Indeed, in the tests this version showed unacceptably low fatigue life of the order of 10^5 current pulses. Here it is calculated for comparison.

2) Horn - Version B (thickness of thin parts increased by 0.4 mm, with the central part being 4 mm thick and 14 mm in diameter) - this version has been chosen and calculated as a final design.

Optimized with respect to the number of focused antiprotons, the horn must be thin and therefore subject to high mechanical stresses, acting dynamically. From the service records of previous horns it is rather clear that their lifetime is limited by mechanical fatigue phenomena, preceding the final failure due to dynamic buckling under compressive electromagnetic forces. The mechanical behavior of the horn is therefore quite complex, and the present analysis is simplified by checking separately the factors influencing the strength of the horn. This included the following points:

a) Estimation of thermal loads generated by electrical current,
b) Static stresses and buckling behaviour under peak electromagnetic forces,
c) Transient dynamic response of the horn to the current pulse,
d) Estimation of the fatigue life of the horn.

The horn is made of high strength aluminium alloy AA 7075 T6, machined from specially prepared forged pieces, ultra-sound controlled before and after machining. For the calculations the guaranteed mechanical properties of the material have been assumed conservatively as: yield strength R_{02} = 430-450 MPa, tensile strength R = 530 MPa, even though the specimens tested at CERN showed superior values. The fatigue properties of this particular material are not available. For typical grades of AA 7075 T6 in extruded state the fatigue limit at 10^7 alternating load cycles (both tension/compression or bending) is usually given as 110 MPa, although much higher values around 160 MPa are also reported in the literature for specific extruded products. As it is typically the case for aluminium alloys, only tests in real condition provide the final verification of fatigue life.

2.2 The Computational Model

The mechanical loads acting on the horn are dynamic in nature. The horn is loaded by pulses of compressive electromagnetic (body) forces, directed perpendicularly to the outer horn surface. As in previous studies [7], these forces have been modelled as surface forces - either as an external pressure (for static and buckling analyses) or as equivalent external concentrated forces (for dynamic analysis). The pressure has been calculated by the approximate formula [6].

$$p = \frac{B^2}{2\pi_0}; \quad B = \frac{\mu_0 I}{2\pi R}$$

with I [A], $\mu_0 = 4\pi \times 10^{-7}$ [H/m], p [Pa], where r [m] is the outer horn radius, changing along the horn. For the horn Version B the pressure varies in the range of 2.8 MPa (thin wide end) to the maximum value of 52 MPa (narrow central part).

The replacement of electromagnetic body forces by the external pressure is justified by the fact that, due to the "skin" effect, the current is concentrated in the outer layer of the horn. The "skin" depth, evaluated under the assumption of the current impulse time (60 μs) being treated as a period of a sinusoidal alternating current (thus for the frequency of ≈16 600 Hz) is of the order of 0.8 - 1.0 mm [8], thus less than a half of the wall thickness of the horn in its thinnest part.

The mechanical computations have been made using the finite element modelling with the ANSYS 4.4 finite element code. The horn has been modelled as an axisymmetric structure with the 4-node harmonic quadrilateral elements allowing for nonaxisymmetric loading. In fact, a rigorous analysis of the mechanical behavior of the horn would necessitate, particularly for a

dynamic analysis, consideration of the whole supporting structure. In the present simplified calculations this has only been taken into account by considering different boundary conditions for the displacements of the horn in axial direction, namely:

a) both horn ends blocked longitudinally,
b) one end blocked, one supported by the (fixed) supporting plate (Fig. 5),
c) one end blocked, one free in longitudinal direction.

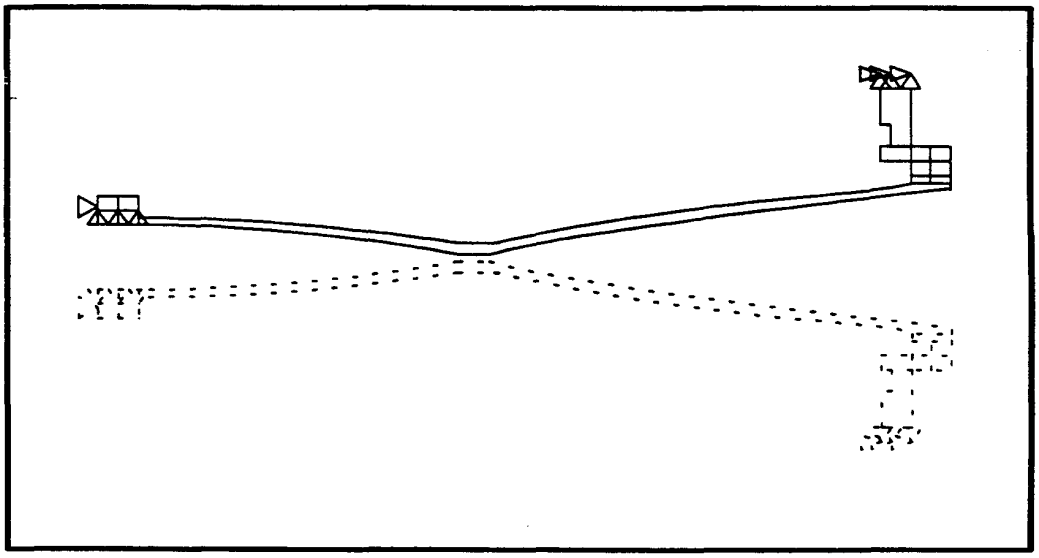

Fig. 5 - Finite element model of the horn-boundary condition (b)

As the axial rigidity of the outer conducting tube is much higher than the horn itself, the real boundary conditions are close to the case (b) or even (a); the case (c) is studied for comparison. This high rigidity also enables the longitudinal electromagnetic force developed in the ends of the supporting structure [6],which in our case is of the order of 1100 daN, to be taken by the outer tube and thus to be neglected in the calculations of the horn.

2.3 Discussion of the Results

2.3.1 Estimation of thermal loads

The heat generated in the horn by one impulse of electrical current is estimated to be of the order of 320 J, calculated by integrating the square of the current over the pulse length, with the electrical resistance of the horn equal to $110 \times 10^{-6}\ \Omega$ (measured for the Horn Version B). The total power of the Joule heating, averaged over the period of current pulse (4.8 s), is therefore of the order of 67 W. This power must be dissipated, mainly by the cooling system of the horn, and also, to a smaller extent, by conduction.

The horn is air-cooled, with the air passing between the horn and the outer housing tube at the flow rate of 300 l/min. The temperature increase of the cooling air, as measured for the horn Version B pulsed at 400 kA, is equal to 7.5 K. This temperature difference corresponds to the power of 45 W which is extracted from the horn by the cooling system. The remaining power of the Joule heating is therefore dissipated by conduction and free convection. The average increase of temperature of the horn, calculated for the above cooling power and with the estimated heat convection coefficient of 20-25 W/(m^{2}K) is of the order of 50 K but may attain higher peak values (70-90 K) during each current cycle. Taking into account that the outer housing tube warms up by some 15-20 K, the average difference of temperature between the horn and the tube is estimated at about 30-35 K.

For such a range of service temperatures (i.e. 340-400 K) the mechanical properties of the horn material are not yet strongly affected, as the aluminium alloy AA 7075 shows abrupt degradation of its properties only at about 430 K, however it points out that a deficiency of the cooling system may lead to a premature failure of the horn by plastic yielding.

The thermal stresses, which may develop as a result of temperature difference between the horn and its supporting structure, are discussed in the following section.

2.3.2. Static stresses and buckling behavior under peak electromagnetic forces

The results of static stress analysis for the three types of boundary conditions are presented in Table 1, where the case of the preliminary horn design (Version A) is also given for comparison. As seen from Table 1 the level of maximum static stresses, which always develops in the central narrow part of the horn, is lower in the case of both horn ends being blocked in axial direction as compared with the horn with no axial restraints.

For the horn Version B the level of static stresses is quite acceptable with respect to limit material properties (typical required safety factor equal to 1.6 with respect to yield strength), at least in the case of boundary conditions (a) and (b). Also the buckling multiplicative factors (or buckling safety factors) are well above the range of safe values, which are typically of the order of 3.5-4.0. This is not the case of the horn Version A which has the safety margins below the required ones.

Table 1 - Summary of static and buckling analysis

HORN VERSION	A		B		
Boundary conditions	(a)	(c)	(a)	(b)	(c)
Maximum eq. von Mises stress [MPa]	262	468	154	177	303
Buckling multiplicative factor	2.9	3.4	5.7	5.7	6.0

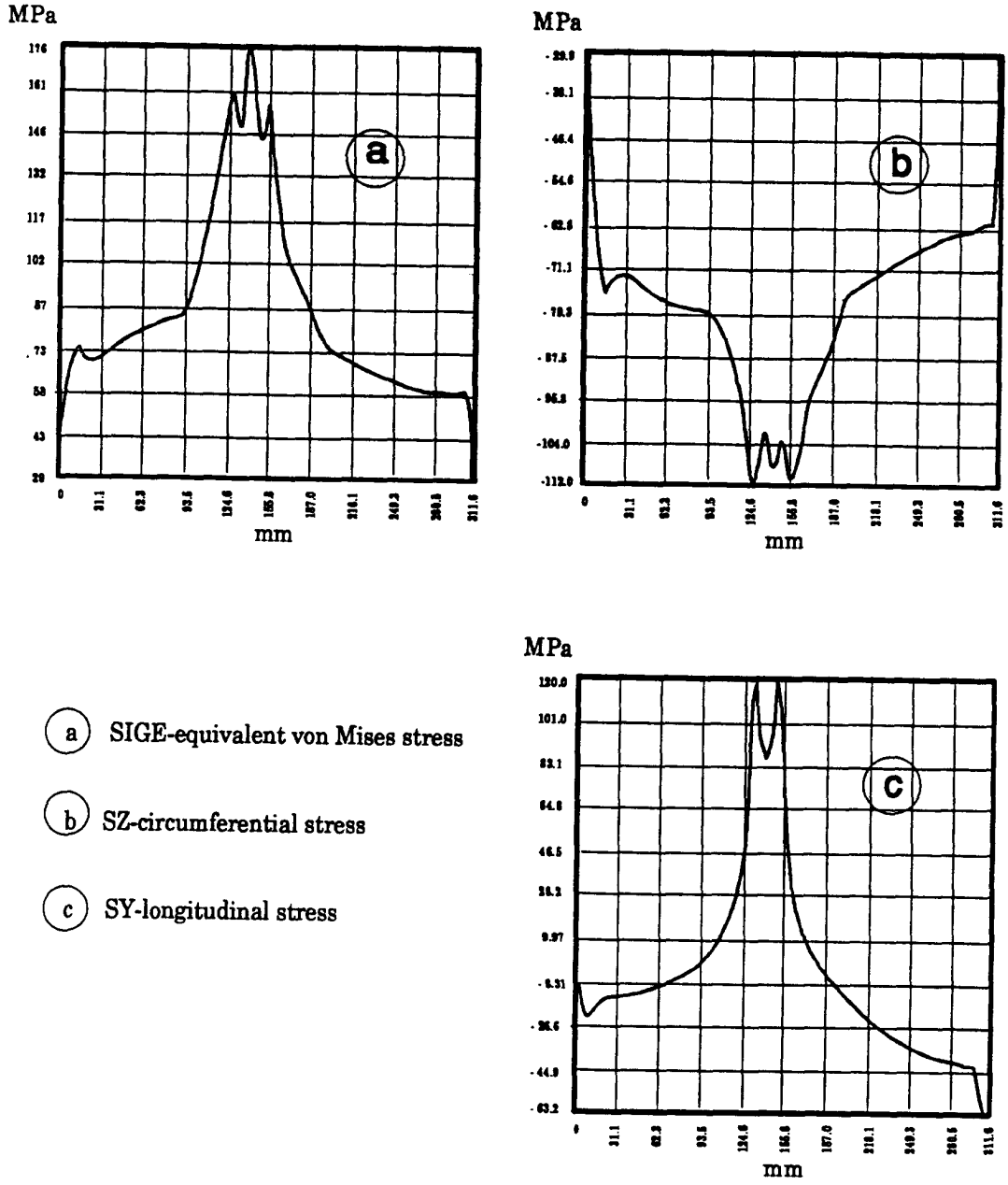

Fig. 6 a,b,c - Static stresses along the horn surface. Boundary condition (b).

It is worth noting that all the calculated buckling factors correspond to the third circumferential mode of buckling, which is obtained as a most probable mode of failure by buckling, just as observed in horn tests. The second observation, which is also worth pointing out, is that quite large tensile longitudinal stresses are developing in the horn, and the main displacements are also in axial direction. The range of stresses for the horn Version B is given in Table 2, the diagrams in Fig. 6 illustrate the changes of stresses along the horn for the second case of boundary conditions.

Table 2 - Range of displacements and stresses for different boundary conditions. Horn Version B - static analysis.

Boundary Conditions		(a)	(b)	(c)
Max. radial displ.	[mm]	-0.012	0.03	-0.027
Max. axial displ.	[mm]	0.058	0.113	0.426
Range of stresses [MPa]				
Radial	- min.	- 58	- 58	- 57
Radial	- max.	29	70	16
Longitudinal	- min.	- 73	- 64	-16
Longitudinal	- max.	87	121	265
Circumferential	- min.	-113	- 110	-109
Circumferential	- max.	4	67	12
Max. equiv. von Mises		154	177	303

The above results of static analysis have been obtained for the horn loaded only by electromagnetic pressure forces. The presence of a temperature difference between the horn and the outer housing tube modifies these results. However, as it has been calculated for the case of boundary conditions (b), closest to real support conditions, this modification is, for the range of temperature difference up to 30-35 K, relatively weak. There is a certain redistribution and shift of stresses toward higher compressive values, but with the global level of stresses remaining nearly the same. In the further analysis the influence of thermal stresses has been neglected.

2.3.3 Transient dynamic analysis

This analysis has been performed to study the dynamic response of the horn (Version B) under impulsive pressure loading. Only single pulse loading has been considered, as it is known from tests that the horn vibrations are attenuated between the current pulses, even though the dumping effects are relatively weak and therefore neglected in the present study. The impulse of electromagnetic forces has been applied as a triangular pulse of external (pressure) forces of total duration of 60 μs, and the vibration behavior of the horn has been calculated with the use of the direct integration method.

The transient dynamic analysis has been preceded by the harmonic analysis of natural frequencies of the horn. For the three cases of boundary conditions studied here, the spectrum of natural frequencies for higher frequency modes, all in kHz frequency range, are quite similar, both for longitudinal and circumferential modes. The lowest frequencies, corresponding to the

axisymmetric mode of deformation, differ, however; for the case (a), i.e. with both ends blocked they equal f_{0m} = 7740, 8518, 8802, ... Hz, for the case (b) of the horn with the supporting plate they are f_{0m} = 4563, 7707, 8737, ... Hz, while for the case (c) of the horn with one end free they are f_{0m} = 481, 2417, 8141, ... Hz.

Table 3 - Range of displacements and stresses for different boundary conditions - Horn Version B - dynamic analysis.

Boundary Conditions	(a)	(b)	(c)
Range of displacements [mm]			
Radial - min.	- 0.021	- 0.021	- 0.041
Radial - max.	+0.009	+0.012	+0.040
Longitudinal - min.	- 0.081	-0.105	- 0.200
Longitudinal - max.	+0.078	+0.108	+0.200
Range of stresses [MPa]			
Longitudinal - min.	- 108	- 107	- 156
Longitudinal - max.	+107	+107	+ 160
Circumferential - min.	- 93	- 93	- 146
Circumferential - max.	+ 43	+ 39	+ 147
Lowest forced frequency [Hz]	8200	4200	2000

There is also a marked difference in the transient dynamic behavior of the horn for the above three cases of boundary conditions (Table 3 and Fig. 7). In the first case (a) the dominating frequency of forced vibrations is around 8 kHz, the dynamic displacements (half-amplitudes) are of the order of static ones, and the maximum dynamic stresses slightly exceed the static ones. A similar tendency is observed for the boundary conditions (b), with the frequency of vibrations around 4 kHz. In the third case (c) there are several superimposed vibration frequencies, the lowest being around 2 kHz, the dynamic displacements are hardly a half of the static ones, and the maximum dynamic stresses are lower than the corresponding static values, but higher than the preceding cases. In all cases for some points of the horn the dynamic stresses may be 2.4-2.5 higher than the static ones, but this is only in the thin horn parts, where these stresses are relatively small.

Summing up the dynamic analysis it may be said that: first, the level of dynamic stresses is in the range of 110 MPa of alternating longitudinal and circumferential stresses, as revealed for the case of boundary conditions (a) and (b), and second, that the case of the horn not supported in axial direction (c) is less favourable, giving higher dynamic stresses.

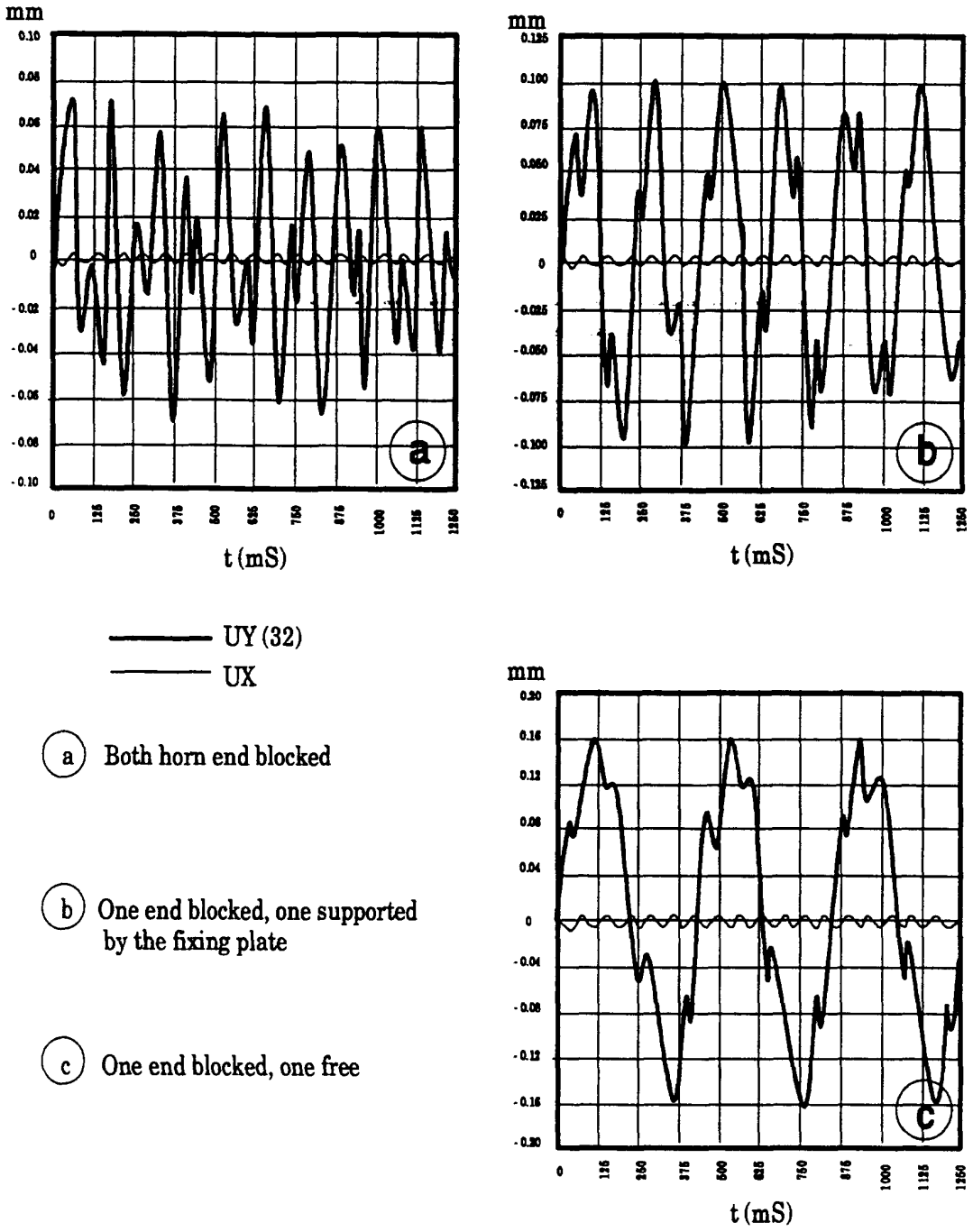

Fig. 7 - Dynamic displacements under impulse of loading for the three types (a,b,c) of boundary conditions. Node 32 - central thin part of the horn. UX= radial displacement, UY= longitudinal displacement.

2.3.4. Estimation of the horn fatigue life

Basing on previous tests of the horns, on the level of calculated static and dynamic stresses and on material fatigue data it is estimated that the fatigue life of the horn (Version B) should be of the order of 7×10^6 current cycles, ensuring one year of continuous service. Given the uncertainty of stress evaluation this estimation must be treated as quite rough and

should be confirmed by further tests of the horns. Although the preliminary horn design (Version A) has not been analyzed with respect to dynamic loads, in this case the level of calculated static stresses suggest a quite low fatigue lifetime, of the order of 10^5 current cycles.

3. HORN PULSER ANALYSIS

In order to generate a current pulse of several hundred thousand Amperes needed for a magnetic horn, a high current pulser has been built at CERN [9, 10]. This pulser uses a capacitor discharge circuit. This principle has the advantage of being simple and reliable but there are some inconveniences. The following calculation is based on a model which outlines the critical points of the circuit. Some malfunctioning effects are described, and the protection against failure is also discussed.

3.1 Description of the System

The pulser (Fig. 8) is composed of 6 distributed capacitor banks (cubicles) with 3 discharging cells in each. Each cell is connected to a current summing box with 4 coaxial cables which are about 100 m long. The connection between the summing box and the load (the magnetic horn) is limited to a big strip line about 8 m long. Physically, the pulser is situated in a non-radioactive zone and only the junction-box, the strip line and the horn are submitted to radiation.

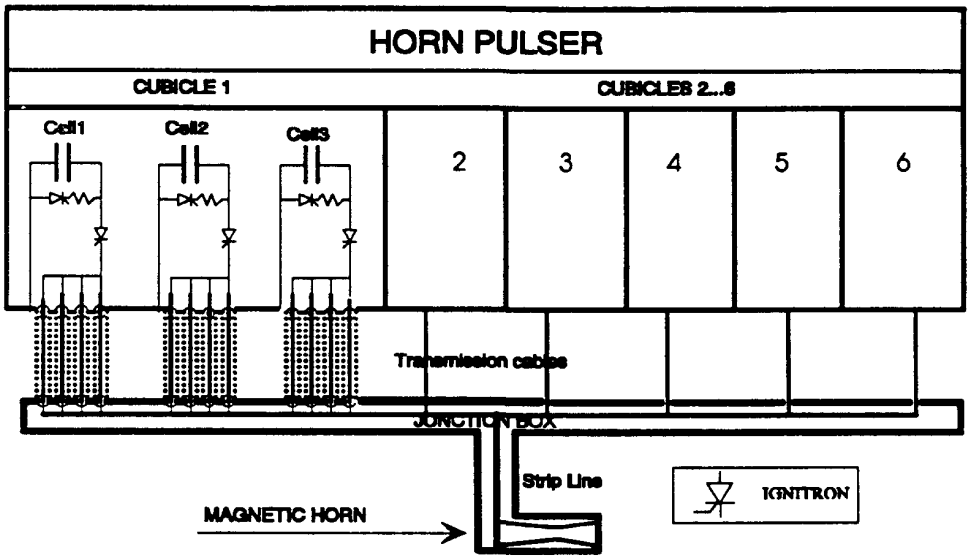

Fig. 8 - General Pulser Layout

The capacitor banks are charged by a dc supply to 5.8 kV and then discharged simultaneously on the load through ignitron switches (mains). The periodic current wave obtained flows through the load, and when the voltage on the capacitors becomes negative a dumping circuit is activated to prevent the negative current flow. Once all the energy has been dumped, a new cycle can start again. The repetition rate of 4.8 s is limited by the current of the dc supply.

3.1.1 Circuit modelling

The model (Fig. 9), which had been elaborated without the transmission line effects and only one RLC cell, simulates the connection between the pulser and the summing box. Because of the low resonant frequency of the circuit, this approximation does not have a large effect. Furthermore, the real measured signals and the results of the simulation show very little difference (Fig. 14).

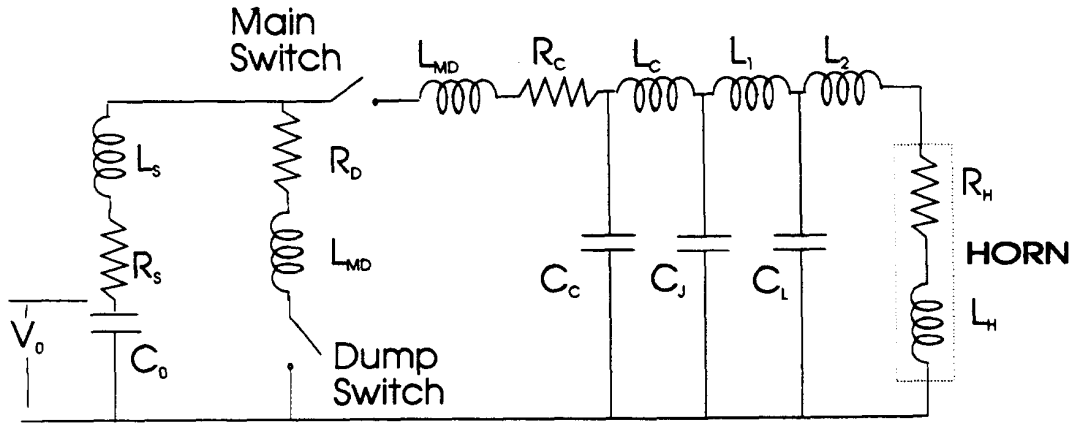

Fig 9 - Model of pulser circuit

Symbols and parameters list:

V_0	Capacitor bank voltage	5800	V
C_0	Equivalent main capacitor	720×10^{-6}	F
R_S	Equivalent capacitor series resistor	5×10^{-3}	Ω
L_S	Equivalent capacitor series inductor	2.5×10^{-9}	H
R_{MD}	Equivalent switch series resistor	0.25×10^{-3}	Ω
L_{MD}	Equivalent switch series inductor	4×10^{-9}	H
R_D	Equivalent dumping resistor	10×10^{-3}	Ω
R_C	Equivalent cable series resistor	0.12×10^{-3}	Ω
C_C	Equivalent cable capacitor	1.44×10^{-6}	F
L_c	Equivalent cable inductors	25×10^{-9}	H
C_J	Stray summing box capacitor	130×10^{-12}	F
L_1	1st part strip line inductor	29×10^{-9}	H
L_2	2nd part strip line inductor	29×10^{-9}	H
C_L	Strip line capacitor	348×10^{-9}	F
R_H	Horn resistor	0.1×10^{-3}	Ω
L_H	Horn inductor	45×10^{-9}	H

Note that the internal switch series resistors are not drawn but are taken into account in the calculation.

3.1.2 Circuit Analysis

The electrical computation has been made using the MICROCAP III [R] program* . The analysis has been done in two phases.

- 1st phase:

For the first phase the circuit is as shown in Fig. 10. At starting time, the capacitor C_0 is charged at V_0 and $I_0 = 0$. When the main switch is closed, the current begins to flow and the simulated analysis (Fig. 11) shows that the circuit is resonant. The main component of the current behaves like a sine with a period of ~60 μs and the amplitude varies with a damping factor $e^{-\alpha t}$ due to circuit resistors.

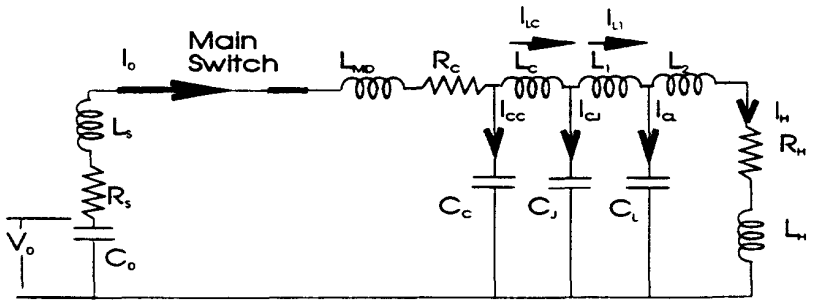

Fig. 10 - Equivalent circuit during the 1st phase

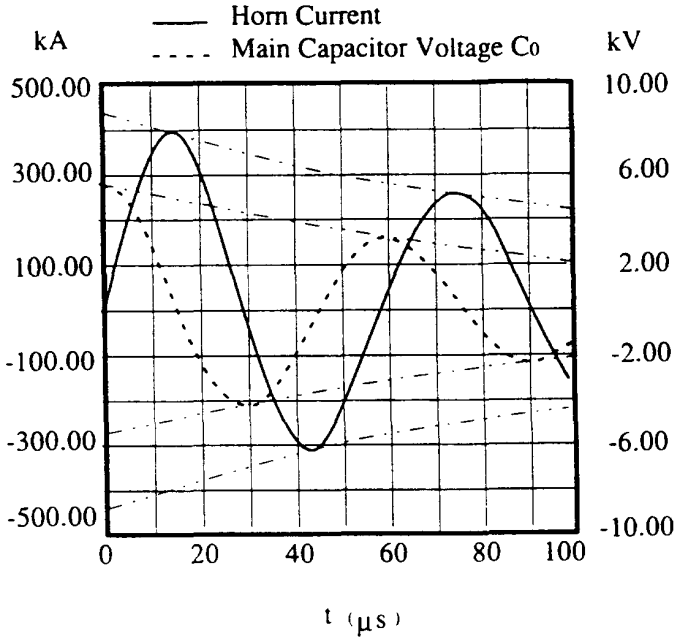

Fig. 11 - Analysis simulation for the first phase

* MICRO-CAP III is a trademark of Spectrum Software by A. Thompson, T. O'Brien, Copyrights 1988-90.

Due to the low horn impedance the current I_0 can be approximated as $\cong I_H$. It is obvious that the circuit has a lot of resonant cells and the real current is composed of multiple oscillations as shown in Fig. 12b. These effects are minimized on the load by L_2+L_H, R_H which acts like a low-pass filter. Furthermore, the top of the pulse is not concerned by the Icc oscillation. (Fig. 10 and Fig 12a).

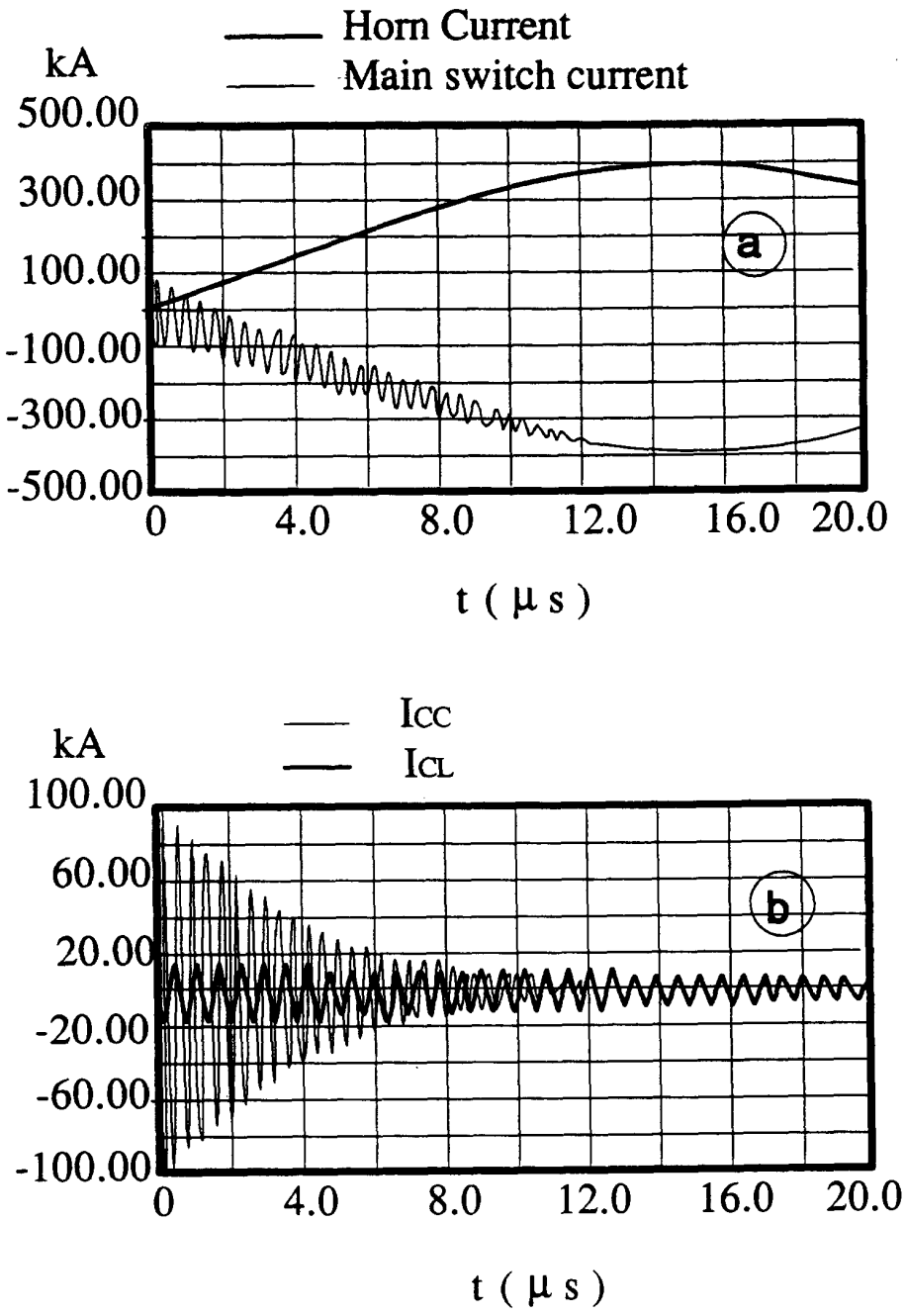

Fig. 12 a,b - Current behavior for I_H, I_0, I_{CC}, I_{CL}

- 2nd phase

As shown in Fig. 11 the voltage across C_0 reverses after 15 μs. At this time we close the dump switch and we modify the circuit parameters (Fig. 13) by introducing the dumping resistor R_D which shunts the current.

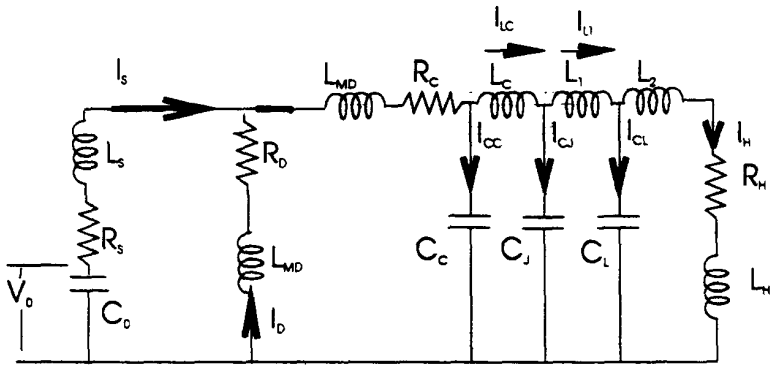

Fig. 13 - Equivalent circuit when the dump switch is closed

Finally the actual current pulse on the horn is shown in Fig.14, and we see that the model is very close to the real circuit.

HORN CURRENT

Model

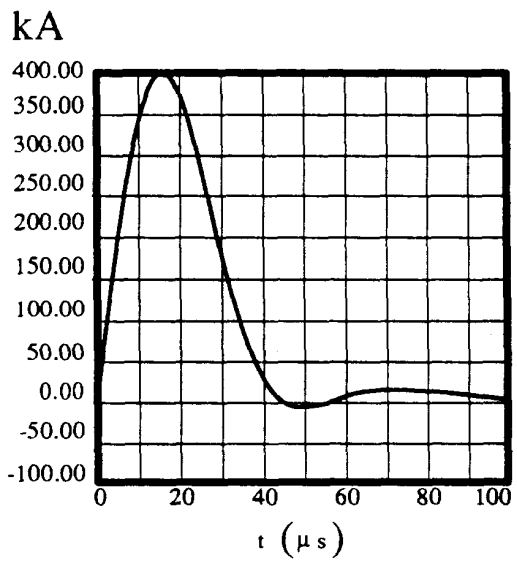

Real circuit

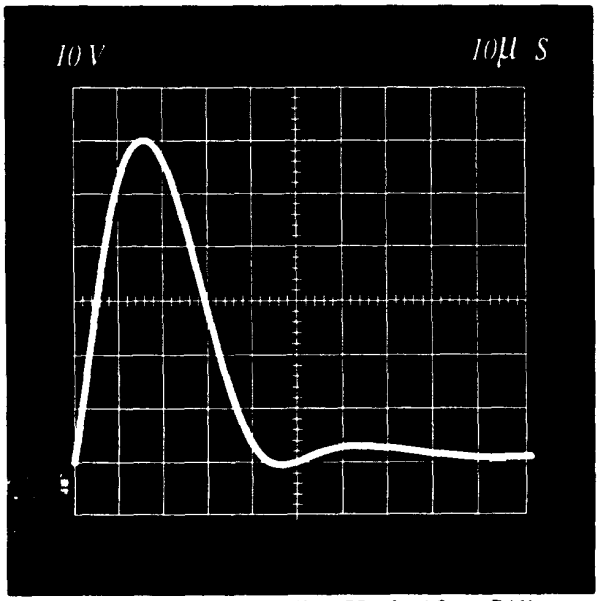

Scale: Vert. 66 kA/div. Horiz 10 μS/div

Fig 14 - Comparaison between the model and the real circuit

3.1.3 Malfunctioning

The previous models suppose that all the switches close simultaneously at the same time. The real pulser circuit has 18 main switches and 18 dump switches. They are of the ignitron type and there is a jitter between them when firing. A computation on a model emulates 2 discharging cells (Fig. 15a,b,c,d) showing that if one cell is triggered 4 μs later its main switch receives an overcurrent of about 20% while the horn current reaches the maximum value 1 μs later. The maximum value changes only by 2.5%. In order to minimize this nasty effect a special firing circuit has been designed which reduces the firing jitter to less than 0.5 μs.

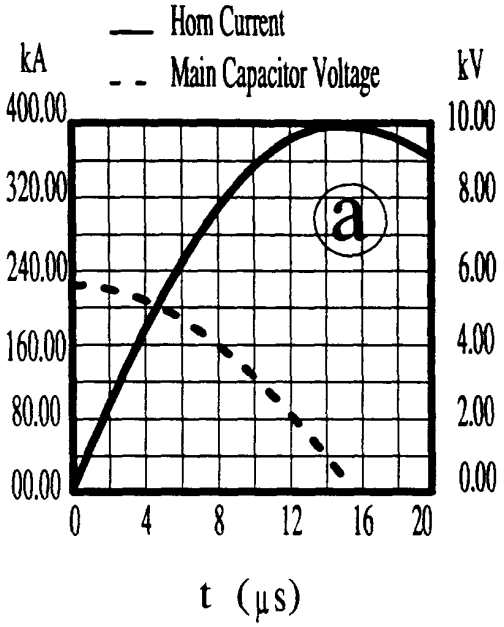

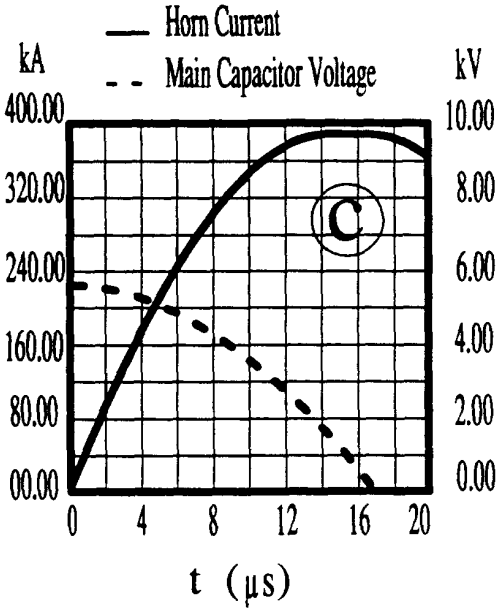

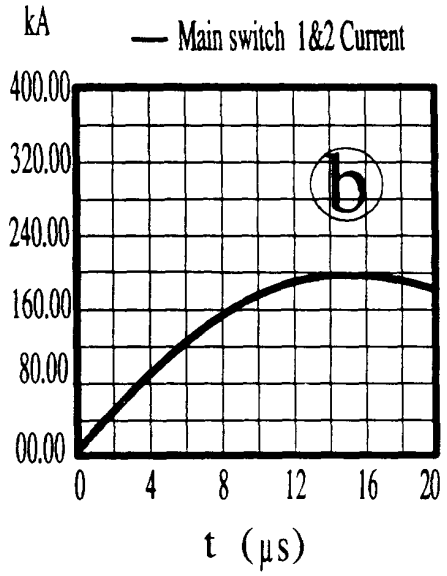

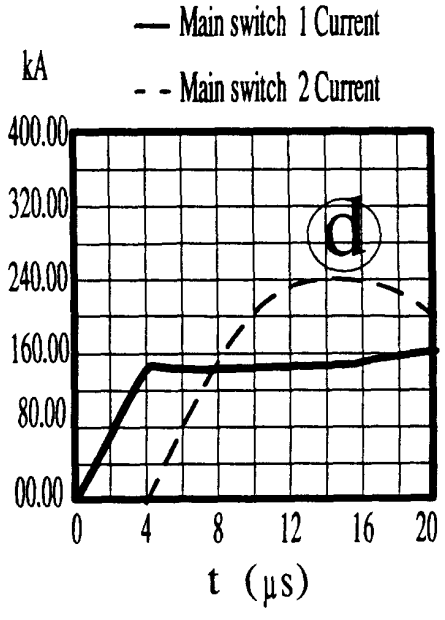

Fig. 15a,b - 2 cells triggered simultaneously

Fig. 15c,d - 2 cells triggered with 4 μs interval

Concerning the dump switches the problem is less critical because they can be fired just before the voltage reversal and they begin to pass the current when the voltage on their anode becomes positive.

3.2 Improvements of the Pulser

In order to minimize the power on the load (the horn) and to prevent reverse current across the switches, the dumping resistor has been chosen accurately. The simulated analysis (Fig. 16) shows the changes of the horn current shape with the variation of the equivalent dumping resistor R_D from 5 to 15 mΩ. The best R_D value is 10 mΩ.

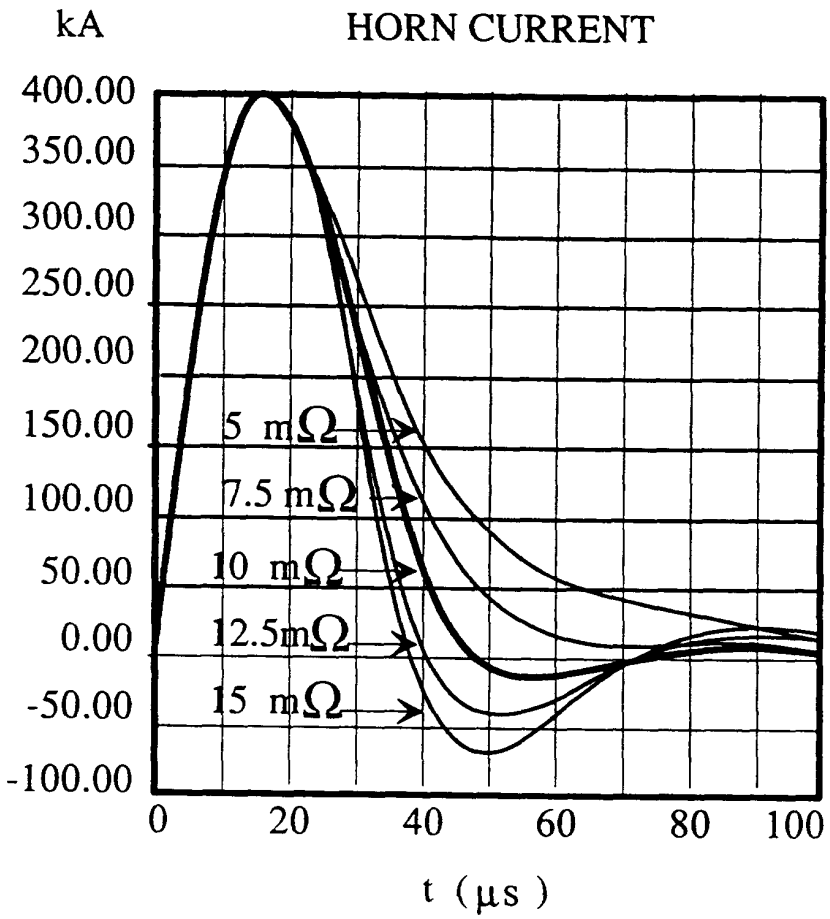

Fig. 16 - Horn current shape with different values of R_D

The main capacitors of the pulser have been changed to 40 μF instead of 60 μF per cell to reduce the length of the current pulse according to the horn calculation requirements, and, consequently, to obtain the required 400 kA, the primary capacitor bank voltage V_0 has been increased from 4.5 kV to 5.8 kV. In order to maintain a good safety factor for the voltage breakdown, all the coaxial connector insulators have been replaced by a new type with 20 kV insulation capability. For the same reason, the long strip-line has been completely re-designed

with new vetronite insulating plates and with the application of a "DAG"[1] to avoid the surface ionization effects. The horn short strip line has also been re-designed with new mica insulating plates and more insulation space.

3.3 Protections Against Failures

3.3.1 Shape surveillance

Due to the high current produced by the pulser, any type of failure has to be prevented because the bad components can be burnt. As discussed earlier, in this pulser configuration, all ignitrons must be fired at the same time. The diagnosis is easy if more than one ignitron fails because the resulting pulse deviates strongly from the desired shape, but it becomes difficult if only one of the eighteen ignitrons fails because the deviation is too small compared to the ideal shape. It is also difficult when the load does not break completely, because the shape of the pulse does not change very much due to the small changes of the "R_H,L_H" values. Moreover, the diagnosis can be complicated if the failure is erratic.

These considerations have contributed to the development of a pulse shape surveillance device [11].

The basic idea is the following: once the preliminary pulser tests are completed and a good current pulse is obtained, the load current signal and the single cell current are sampled with a fast ADC. The acquired values are stored in a memory. This action is done once and the values contained in the memory become the reference values for comparison at each of the following pulses. If a difference is detected, an error signal is produced and reported for the appropriate stop action.

3.3.2 Temperature surveillance

It is known that the temperature of the horn during pulsing is not very far from the temperature limit where the degradation of the aluminium properties starts. To avoid an early failure of the horn by plastic yielding, the horn temperature is continuously recorded by measuring the temperature difference between the inlet and the outlet of the air cooling flow. A trip occurs if the safety limit is exceeded.

4. EXPERIMENTAL RESULTS

4.1 Effects of the Higher Thickness on the Horn Efficiency

The antiprotons, from the target, pass through the horn material before they exit in a parallel beam (Fig. 1). Even with a light aluminium alloy, the particles undergo re-absorption

---

[1] The "DAG" is a semiconducting paint

and multiple Coulomb scattering [6]. The effect of a thicker magnetic horn on the yield has been calculated and summarised in Table 4 and Fig. 17 with

Δs : the additional thickness along the horn (mm),
$L(s)$: the total traversal length (cm),
ε_{ms} : the multiple Coulomb scattering efficiency,
ε_{abs} : the absorption efficiency,
ε : the global efficiency,
$\varepsilon(s)/\varepsilon(0)$: the global efficiency relative to the efficiency with $\Delta s = 0$.

Table 4 - Effect of a higher thickness on the yield

Δs	$L(s)$	$\varepsilon_{ms}(L(s))$	$\varepsilon_{abs}(L(s))$	$\varepsilon(s)$	$\varepsilon(s)/\varepsilon(0)$
-0.2	29.858	0.861	0.923	0.795	1.019
-0.1	31.077	0.856	0.92	0.787	1.01
0	32.297	0.85	0.917	0.78	1
0.1	33.516	0.845	0.914	0.772	0.991
0.2	34.736	0.84	0.911	0.765	0.981
0.3	35.956	0.835	0.908	0.758	0.972
0.4	37.175	0.829	0.905	0.751	0.963
0.5	38.395	0.824	0.902	0.744	0.954
0.6	39.614	0.819	0.899	0.737	0.945
0.7	40.834	0.814	0.896	0.73	0.936
0.8	42.053	0.809	0.893	0.723	0.927
0.9	43.273	0.804	0.89	0.716	0.919
1	44.492	0.8	0.887	0.71	0.91

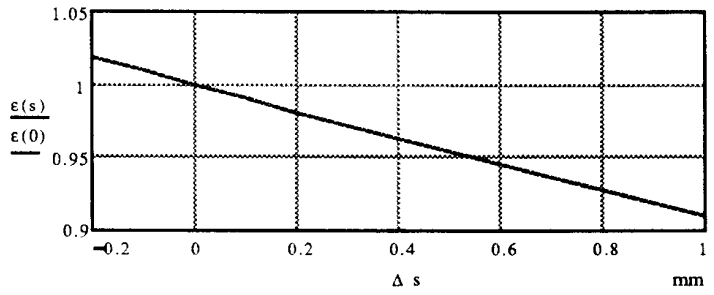

Fig. 17 - Diagram of the relative efficiency as a function of Δs

From the theoretical calculation we notice that the effect of the thicker horn on the yield is quite small and, in our particular case, with an additional 0.4 mm thickness, the yield is lower by 4%.

4.2 Injection Line Matching [12]

The antiprotons produced in the target and collected by the magnetic horn are transported and matched through the injection line to the collector ring.

The injection line has been designed to match the antiproton collector (36 mm Li lens) to the AC machine and to have a transverse acceptance of 240π mm·mrad and a momentum acceptance of 6%. With a collector of a larger diameter (60 mm magnetic horn), the beam size was so large, in particular in the dipoles in the vertical plane, that it was not possible to transmit 240π mm·mrad. A transverse acceptance of 200π mm·mrad was retrieved after modification of the matching conditions at the exit of the collector. In particular the Twiss parameter, α was small but no longer zero, which means that the beam is not parallel at the exit of the horn.

4.3 Experimental Yield Measurements

The experience confirmed the theoretical prediction. The thicker horn was put into the AAC target area and the yield was measured. Figures 18a, b, c show a comparison between yield measurements of 3 different types of collector, the value of the transformer TFA5308 at the end of the injection line and the value of the transformer TFA9053 which is located before the target and giving the number of protons on the target.

The mean value of the yield measurement of the Li lens over a long period (several months) is about 56×10^{-7} instead of 50×10^{-7} for the previous magnetic horn and for the thicker one over a period of 2 weeks [13].

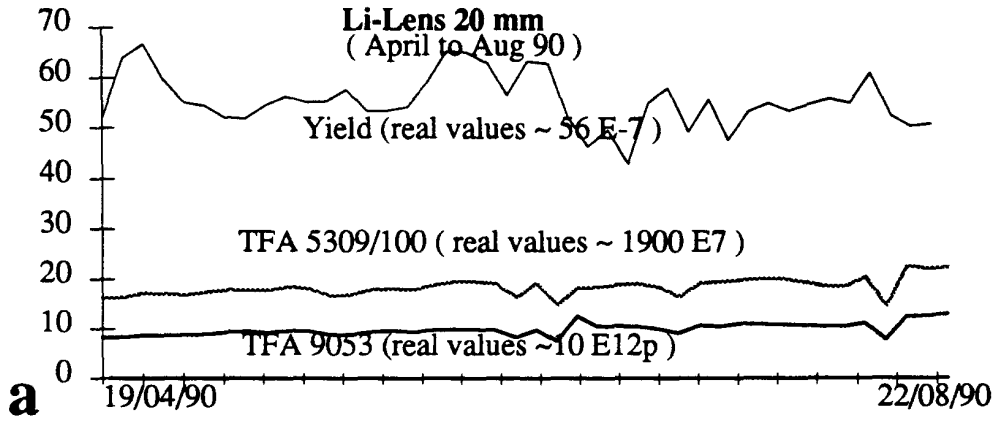

Fig. 18a) - 20 mm Li lens yield measurement

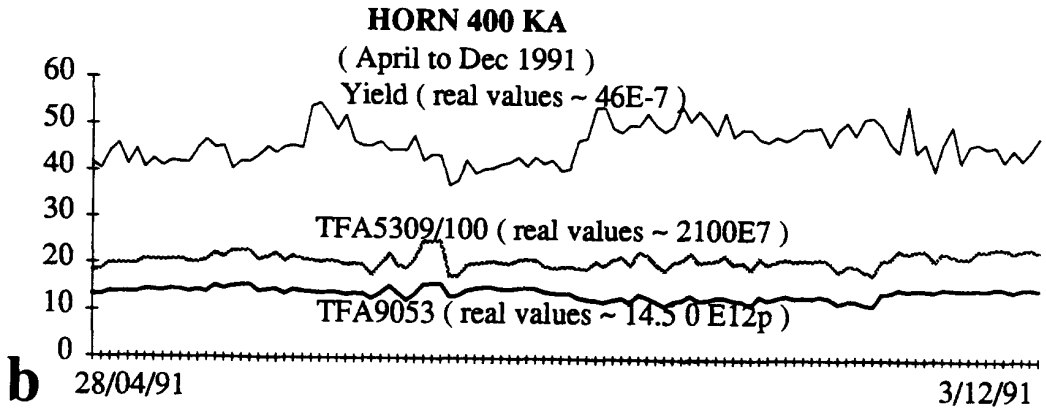

Fig. 18b) - 400 kA standard horn yield measurement

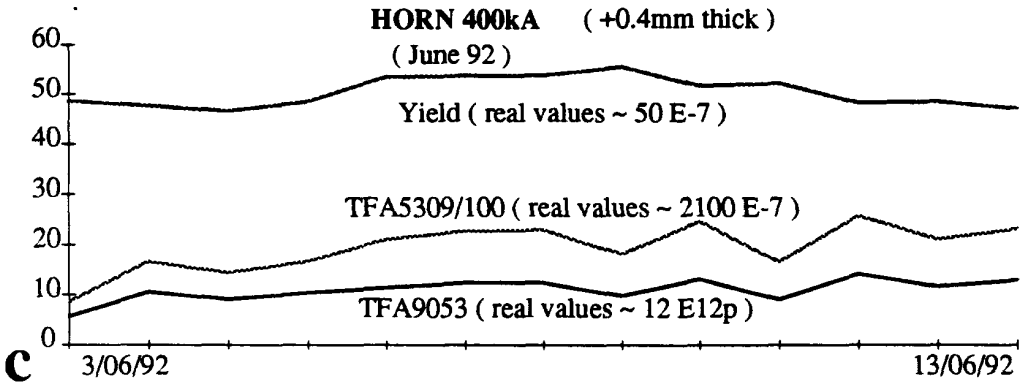

Fig. 18c) - 400 kA Horn (+0.4 mm thick) yield measurement

There is no significant difference between the 2 magnetic horn performances. The Li lens performance is only shown for completeness.

4.4 Laboratory Tests Summary

The results of the different laboratory tests are given in Table 5.

Table 5

HORN Number	Test Date	Type of material	Origin of material	Tooling	Design	Remarks	Final test results
0	07/91	Fortal 7075 extruded	AL-METAL France	Apretec Lyon	Original	No ultrasonic test	Break at 90.000 cycles
1	01/92	Perunal 215 extruded	Menziken CH	Apretec Lyon	Original	Ultrasonic and Metall. test OK	Break at 50.000 cycles
2	01/92	Fortal 7075 extruded	AL-METAL France	Apretec Lyon	Original	Ultrasonic and Metall. test OK	Break at 26.000 cycles
3	02/92	Perunal 215 compressed	Fabr. Fed. d'avions CH	Mecatest Geneva	Original	Ultrasonic and Metall. test OK	Break at 33.000 cycles
4	02/92	Perunal 215 compressed	Fabr. Fed. d'avions CH	Mecatest Geneva	Original	Ultrasonic and Metall. test OK	Not tested, Out of tooling specification.
5	04/92	Perunal 215 extruded	Menziken CH	Mecatest Geneva	Thick. + 0.4	Ultrasonic and Metall. test OK	Not tested, Out of tooling specification.
6	08/92 10/93	Perunal 215 compressed	Fabr. Fed. d'avions CH	Mecatest Geneva	Thick. + 0.4	Ultrasonic and Metall. test OK	500.000cycles at 400 KA in 92 after screws change from M5 to M6 500.000cycles at 500 KA. in 93
7	04/92	Perunal 215 compressed	Fabr. Fed. d'avions CH	Apretec Lyon	Thick. + 0.4	Ultrasonic and Metall. test OK	100.000cycles at 400 KA 100 cycles at 480 KA. Installed in the target area, screws failure after 250.000 cycles
8	04/92	Perunal 215 extruded	Fabr. Fed. d'avions CH	Mecatest Geneva	Thick. + 0.4	Ultrasonic and Metall. test OK	Not tested, used as tooling model
9	01/93	Perunal 215 extruded	Menziken CH	Apretec Lyon	Thick. + 0.4	Ultrasonic and Metall. test OK	1.000.000 cycles at 400 KA and after screws modification from M5 to M6 100.000 cycles at 400 KA Kept as SPARE n. 3
10	Does not exist						
11	02/93	Perunal 215 compressed	Fabr. Fed. d'avions CH	Mecatest Geneva	Thick. + 1.0	Ultrasonic and Metall. test OK	150.000 cycles at 400 KA Flanges of 10mm screws M6
12	02/93	Perunal 215 compressed	Fabr. Fed. d'avions CH	Apretec Lyon	Thick. + 1.0	Ultrasonic and Metall. test OK	Not tested Flanges of 10mm screws M6
13	08/93	Perunal 215 CH921 Forged	Fabr. Fed. d'avions CH		Thick. + 0.4	Ultrasonic and Metall. test OK	500.000 cycles at 400 KA Flanges of 10 mm screws M6 Kept as SPARE n. 1
14	09/93	Perunal 215 CH921 Forged	Fabr. Fed. d'avions CH		Thick. + 0.4	Ultrasonic and Metall. test OK	500.000 cycles at 400 KA Flanges of 10 mm screws M6 Kept as SPARE n. 2

CONCLUSION

As explained in the introduction, the first unit installed in the target area was pulsed for about 2 million cycles before the coaxial box and the screws broke. Initially, it appeared it was only necessary to rebuild some spares with the same design. Unfortunately, all the lifetime tests made in the laboratory on the new units were very short and failed between 50 and 100 thousand cycles.

Further laboratory tests have been pushed forward to find a reliable solution for the construction of magnetic horns. A well-defined procedure has therefore been introduced for the choice of the materials. All the primary aluminium rods were submitted to an accurate analysis by the metallurgy service in order to point out any internal defaults. Different methods of manufacturing and different thermal treatments were used in some cases (extruded FORTAL 7075 and extruded, compressed, forged PERUNAL 215). Despite the best material chosen, all the units of the original design failed after a few thousand pulses during the electrical tests.

Investigations on the mechanical stresses imposed to the horn have shown that the mechanical loads were underestimated in the original design [14, 15]. The calculated lifetime of a horn pulsed at 400 kA was of the order of 100 000 pulses, in good agreement with the laboratory tests. In the light of this experience, the long lifetime of the first horn used for the antiproton collection is not fully understood.

Despite a theoretical estimation of 4% yield decrease, the thickness of the horn was increased by 0.4 mm. Two samples were manufactured and electrically tested for more than 100 000 pulses without any failure. The new horn was installed in the beam and no significant change in yield was observed which confirms the calculation. After 250 000 pulses the horn itself had resisted to the mechanical loads, but the assembly screws between the flange and the box broke due to mechanical stresses which had also been underestimated.

The thickness of the flanges has been increased from 6 to 10 mm, the diameter of the screws from M5 to M6, and the box containing the horn has also been reinforced.

Taking into account the design of the new horn and its assembly, the result of the mechanical analysis gives now a safety factor of the order of 3.5-4.0 and, finally, the new magnetic horn has been successfully pulsed up to 1 million cycles in the laboratory. One unit has been pulsed, for test purposes, to a current of 500 kA, which represents 25% more than the normal operating load, for 500 000 cycles without any problems.

A new automatic air cooling system has been introduced to allow the replacement of the horn in the highly radioactive environment without human intervention.

Finally, the effect of the radioactivity on the lifetime of high pulsing devices is not known. Further investigations about the influence of ionizing particles on the crystalline webb

of the material were pushed forward, but our knowledge is still limited to steel alloys used for nuclear farms and under neutrons [16].

All these improvements give reliable magnetic horns in the laboratory, but complete results will be only obtained by the implementation of the collector in the AAC target area.

To-day:

- 6 spares are ready to be installed in the machine for the antiproton operation,
- 2 manufactured horns will be available in the near future,
- 2 pulsers, strip lines and summing boxes are available,
- 2 fully assembled "horn chariots" are ready for operation and one is ready for tests in the laboratory.

The material can be obtained from two suppliers and the experience for tooling the horns is shared between 3 manufacturers. All the documentation necessary to rebuild any pieces of the 400 kA magnetic horn system is available [17].

ACKNOWLEDGMENTS

The magnetic horn consolidation has been pushed forward to insure the future of the antiproton physics. This job has involved a full cooperation between specialists in different fields, Divisions and Groups. The final success could not be achieved without them. We would like to thank J.C. Godot, B. Jenny, G. McMonagle, A. Poncet, C.Scheffre, H. Therville, B. Williams, and the CERN metallurgy service for their constant support and fruitful collaboration.

REFERENCES

[1] B. Autin, G. Carron, F. Caspers, V. Chohan, C.D. Johnson, E. Jones, G. Le Dallic, S. Maury, C. Metzger, D. Möhl, Y. Orlov, F. Pedersen, A. Poncet, J.C. Schnuriger, T.R. Sherwood, C.S. Taylor, L. Thorndahl, S. van der Meer, and D.J. Williams, *Antiproton Accumulator Complex (AAC) Performance*, Proc. of EPAC'90, p. 614.

[2] R. Bellone, C.D. Johnson, G. Le Dallic, M. Lubrano di Scampamorte, S. Maury, C. Metzger, F. Pedersen, T.R. Sherwood, P. Sievers, F. Völker, N. Walker, and G. Silvestrov (INP-Novosibirsk), *Beam Tests of a 36 mm Lithium Lens*, Proc. of EPAC'90, p. 1303.

[3] J.-C. Schnuriger, *Formulae for Antiproton Production Optics*, CERN/PS/85-55 (AA), 1985.

[4] Design Study Group, *Design Study of a Proton-Antiproton Colliding Beam Facility*, CERN/PS/AA 78-3, 1978.

[5] J.-C Schnuriger, *Proposal for a Reliable Solution of the Improved Production of Antiprotons for ACOL*, PS/AA/ACOL Note 21, 1984.

[6] J.-C. Schnuriger, *A Collection of Accelerator Algorithms for the Personal Computer*, PS/AR Note 93-12, 1993.

[7] A. Poncet, *Calculs de comportement dynamique de la corne AA sous charge impulsionnelle*, Note PS/AA/AP/81-1, 1981.

[8] H. Knoepfel, *Pulsed High Magnetic Fields*, North-Holland, Amsterdam 1970.

[9] G. Lebee, *Corne AA*, Note CERN/EP/81-03, 1981.

[10] P. Coventry and D.Fiander, Private comunications.

[11] R. Maccaferri, *Pulse Shape Survey*, Note CERN/PS/BT/86-3, 1986

[12] S. Maury, *How Well Can We Collect Antiprotons with a Big Horn (60 mm in Diameter) and a Small Lithium Lens (20 mm in Diameter) in the ACOL Dogleg*, PS/OP/Note 85-35, 1985.

[13] G. Adrian and V. Chohan, *Operational Performance of the Different Collector Lenses After the Target of the AAC Complex (1989-1992)*, PS/OP/Note 93-59 (Tech), 1993.

[14] J.-C. Godot, *Calculs corne magnétique avec Bosor 1992*, Internal Note, 8.9.1992

[15] B. Jenny, *Calculs corne ACOL 400 kA*, Memo/MT-ESH/BJ, 22.5.1992.

[16] J.J. Chêne, *Bombardement neutronique des métaux*, EPFL/letter , 23 november 1992

[17] M. Lubrano di Scampamorte, *Dossier technique des cornes magnetiques 400 kA*, CERN/MT/Drawings record files, 1993.